Nano Research

Open Access

Research Article

Amino-terminated polydimethylsiloxane modified porphyrin for efficiently biphasic photosynthesis of H_2O_2

Ji Liu[1,§], Hengjun Shang[1,§], Wenting Qiu[1], Shuai Dou[1], Yaning Zhang[1], Jing Xu[2], Jiawei Zhang[1], Yang Lou[1], Ying Zhang[1], Yongfa Zhu[3], and Chengsi Pan[1] ✉

[1] *International Joint Research Center for Photoresponsive Molecules and Materials, School of Chemical and Material Engineering, Jiangnan University, Wuxi 214122, China*
[2] *School of Food Science and Technology, Jiangnan University, Wuxi 214122, China*
[3] *Department of Chemistry, Tsinghua University, Beijing 100086, China*
[§] *Ji Liu and Hengjun Shang contributed equally to this work.*

Cite this article: *Nano Research*, **2026**, *19*, 94908474. https://doi.org/10.26599/NR.2026.94908474

ABSTRACT: Hydrogen peroxide (H_2O_2) attracts widespread attention as a clean and sustainable oxidant. Nevertheless, porphyrin-based photocatalysts generally exhibit low H_2O_2 concentration in aqueous systems because the generated H_2O_2 does not accumulate effectively and is difficult to separate from the water. Here, we report an amino-terminated polydimethylsiloxane (NH_2-PDMS) modified supramolecular tetrakis(4-carboxyphenyl) porphyrin (SA-TCPP) for effectively photocatalytic H_2O_2 production in a water/n-decane biphasic system. We illustrate that the formation of amide bonds (–CO–NH–) between NH_2-PDMS and SA-TCPP regulates the catalyst's surface from hydrophilic to hydrophobic, enabling its uniform dispersion in the nonpolar (*n*-decane) organic phase. We further demonstrate that this spatial distribution effectively separates the NH_2-PDMS@SA-TCPP catalyst from the generated H_2O_2, allowing H_2O_2 to accumulate in the aqueous phase and reducing its decomposition. The NH_2-PDMS@SA-TCPP catalyst delivers an H_2O_2 generation rate of 10.5 mM·h^{-1} and an apparent quantum efficiency as high as 16.02% at 420 nm. Additionally, in a long-term run, the accumulation of H_2O_2 with concentration is found to reach ca. 0.65 wt.%, close to the commercial level (1 wt.%–3 wt.%). This biphasic design provides a simple approach for efficient, stable, and sustainable H_2O_2 production.

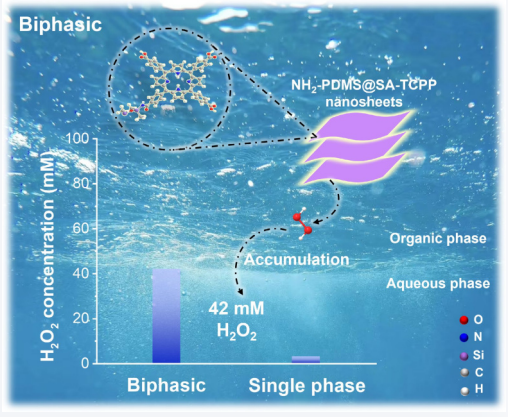

KEYWORDS: hydrogen peroxide, porphyrin, amino-terminated polydimethylsiloxane, biphasic

1 Introduction

Hydrogen peroxide (H_2O_2) serves as a clean and versatile oxidizing agent, extensively utilized in medical treatment, environmental purification, and green synthesis [1–3]. At present, the industrial H_2O_2 is synthesized through the anthraquinone (AQ) route, it remains energy-demanding, produces toxic by-products, and raises concerns regarding the storage and transportation of unstable H_2O_2 solutions [4–6]. Photocatalytic synthesis is gained prominence as a sustainable, sunlight-driven strategy that converts simple substrates—typically water and oxygen—into H_2O_2 using a semiconductor catalyst. However, the practical application of photocatalytic H_2O_2 production still encounters multiple challenges [7–9].

Beyond intrinsic catalytic constraints such as inefficient charge separation, the separation and accumulation of H_2O_2 remain the primary bottlenecks to scaling photocatalytic H_2O_2 production [10, 11]. First, in conventional single-phase systems, the separation of H_2O_2 from the catalyst requires additional energy input, resulting in considerable economic costs. Second, the attainable H_2O_2 concentration in the aqueous phase is low because the generated H_2O_2 readily undergoes decomposition or side reactions on catalyst surfaces and in water, which prevents its effective accumulation. The introduction of a biphasic photocatalytic system may spatially separate the generated H_2O_2 away from the catalyst, minimizing contact with active sites to suppress decomposition and enabling effective H_2O_2 concentration and extraction.

Received: November 21, 2025; **Revised:** January 15, 2026
Accepted: January 21, 2026

✉Address correspondence to cspan@jiangnan.edu.cn

In reported biphasic systems, benzyl alcohol [12–14] and 1-octanol [15] are often used as the organic phase. However, they serve as sacrificial donors and are readily oxidized by H_2O_2. They often partially dissolve organic semiconductor catalysts, break their intermolecular structure, decrease the H_2O_2 production activity. To overcome these issues, chemically inert organic solvents such as toluene [16] and dichloromethane [17] are introduced alternatively. Their inertness suppresses undesired oxidation and side reactions, providing a controlled reaction environment and improving H_2O_2 stability. Nevertheless, their relatively low boiling points and toxicity limit their use under the thermal effects induced by light irradiation. Hence, the organic phase in an efficient biphasic system should be chemically inert, immiscible with water, low-cost, and low-toxic.

The n-decane [18, 19] may be selected as the organic phase because it is chemically stable and unreactive toward the generated H_2O_2, while its relatively high boiling point (174 °C) minimize photothermal evaporation and ensure stability and reproducibility of the system.

In our previous work, we reported that self-assembled tetrakis(4-carboxyphenyl) porphyrin (SA-TCPP) nanosheets exhibited outstanding photocatalytic performance, with an extended absorption range into the near-infrared region and an impressive H_2O_2 generation rate of up to 1.72 mM·h^{-1} [20]. Therefore, incorporating SA-TCPP into a biphasic photocatalytic system is expected to further increase the H_2O_2 performance in the system. When constructing such a biphasic system, the interaction between the photocatalyst and the biphasic solvent plays a decisive role in determining overall efficiency [21, 22]. Note that SA-TCPP contains abundant carboxyl groups and exhibits strong hydrophilicity, making it difficult to be stably introduced into an organic photocatalytic system. To improve its organic compatibility, polydimethylsiloxane (PDMS) is introduced as a surface modifier owing to its high transparency, hydrophobicity, and chemical inertness [23]. Nevertheless, pristine PDMS [24] interacts with SA-TCPP only through physical forces, leading to the aggregation of SA-TCPP within the PDMS matrix and hindering the formation of a stable hybrid structure. Amino-terminated polydimethylsiloxane (NH_2-PDMS) [25] is expected to form covalent amide linkages (–CO–NH–) with the carboxyl groups of SA-TCPP, which may help the dispersion of SA-TCPP in the organic phase.

Here, we developed a water/n-decane biphasic photocatalytic system employing amino-functionalized polydimethylsiloxane-modified self-assembled TCPP (NH_2-PDMS@SA-TCPP) as the active photocatalyst. We systematically investigated the H_2O_2 production performance on the prepared NH_2-PDMS@SA-TCPP. In particular, controlled photocatalytic experiments were conducted to evaluate the influence of key operational parameters, including reaction temperature, water/n-decane volume ratio, NH_2-PDMS/SA-TCPP mass ratio, and solvent polarity. To further elucidate the reaction environment, we integrated *in situ* spectroscopic characterization with phase-distribution tracking to monitor the formation and migration of H_2O_2 within the biphasic medium. This methodological framework was employed to clarify how molecular modification and reaction conditions regulate the pathways of photocatalytic H_2O_2 generation, thereby providing guidance for the rational design of efficient biphasic photocatalytic systems.

2 Experimental

2.1 Preparation of SA-TCPP

TCPP (150 mg) was dissolved in 5 mL of 0.5 M KOH and stirred for 30 min at ambient temperature. The alkaline solution was slowly titrated with 0.1 M HCl from a constant-pressure funnel until the pH reaches approximately 4.0. The resulting solid was isolated by centrifugation and rinsed three times with deionized water until the supernatant becomes neutral. The obtained SA-TCPP powder was subsequently dried at 60 °C for 12 h.

2.2 Preparation of NH_2-PDMS modified SA-TCPP catalyst

The NH_2-PDMS (0.3–0.9 g) was first dissolved in 20 mL of n-heptane under vigorous stirring to obtain a homogeneous solution. The SA-TCPP supramolecular material was then introduced, and the suspension was stirred at 100 °C for 1 h to achieve surface modification. The resulting composite was collected by centrifugation and dried at 80 °C to yield the NH_2-PDMS@SA-TCPP catalyst.

2.3 Photocatalytic production of H_2O_2

In the photocatalytic H_2O_2 generation, 45 mg of NH_2-PDMS@SA-TCPP catalyst was dispersed in 30 mL of reaction medium (water:n-decane = 1:5) within a quartz reactor. Oxygen was purged through the suspension for 30 min in the dark. The reactor was then placed in a thermostatic oil bath maintained at 80 °C and irradiated with a 300 W Xe lamp (150 mW·cm^{-2}, $\lambda \geq 420$ nm).

The concentration of H_2O_2 was quantified using the potassium titanium oxalate method. At predetermined intervals, 1 mL of the reaction mixture was withdrawn through a 0.45 μm syringe filter and combined with 1 mL of 0.02 M potassium titanium oxalate solution. A transparent-to-yellow color change indicated complexation between titanium oxalate and H_2O_2. The absorbance at 400 nm was recorded with a ultraviolet–visible (UV–Vis) spectrophotometer (UV-9010, Pushi, China) to determine the H_2O_2 concentration.

3 Results and discussion

3.1 Morphological and structural characterizations

The morphology of the prepared samples was characterized by scanning electron microscopy (SEM), transmission electron microscopy (TEM), and atomic force microscopy (AFM). As shown in Fig. 1(a), the SEM image of NH_2-PDMS@SA-TCPP exhibits a uniform and smooth surface with a diameter of 0.2–2 μm. Compared with pristine SA-TCPP (Fig. S1 in the Electronic Supplementary Material (ESM)), the overall morphology remains nearly unchanged, indicating that the introduction of NH_2-PDMS does not disrupt the supramolecular self-assembly. This observation was further confirmed by the TEM images of SA-TCPP and NH_2-PDMS@SA-TCPP (Figs. S2(a) and S2(b) in the ESM). Both samples display thin sheet-like structures, while the NH_2-PDMS@SA-TCPP nanosheets exhibit an average thickness of about 3.72 nm (Fig. 1(b)), slightly thicker than pristine SA-TCPP (3.40 nm) [20] due to the presence of surface-grafted NH_2-PDMS chains. This result verifies that NH_2-modified polydimethylsiloxane (NH_2-PDMS) introduced into SA-TCPP did not alter its inherent two-dimensional morphology, and the supramolecular assembly shows

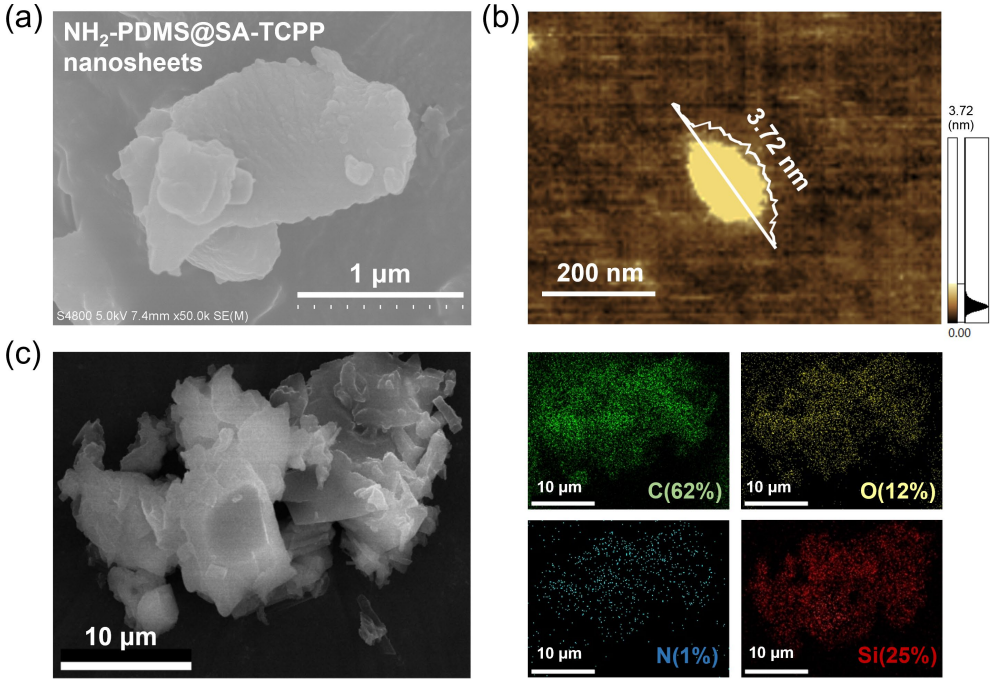

Figure 1 (a) SEM, (b) AFM, and (c) SEM-EDS elemental mapping images (C, O, N, Si) of NH_2-PDMS@SA-TCPP catalyst.

good consistency in the powder X-ray diffraction (PXRD) patterns (Fig. S3 in the ESM).

The SEM-EDS elemental mapping (Fig. 1(c)) shows homogeneous distributions of C, O, N, and Si, confirming the coexistence of the SA-TCPP nanosheet and NH_2-PDMS. The well-dispersed Si signal directly demonstrates that NH_2-PDMS is uniformly anchored on the SA-TCPP surface. Quantitative EDS analysis (62% C, 1% N, 12% O, 25% Si), combined with the molecular weight of NH_2-PDMS measured by gel permeation chromatography (GPC) (M_P approximately 6833 g·mol^{-1}, corresponding to ca. 92 Si atoms per chain, Fig. S4 in the ESM), indicates that NH_2-PDMS@SA-TCPP contains roughly one NH_2-PDMS chain per SA-TCPP molecule.

These results collectively indicate that NH_2-PDMS preferentially resides on the outer surface of the SA-TCPP nanosheets. The presence of this semi-solid siloxane layer preserves the nanosheet morphology, which may help maintain structural integrity during subsequent photocatalytic reactions.

The interaction between SA-TCPP and NH_2-PDMS was investigated by Fourier transform infrared (FTIR) spectroscopy (Fig. 2(a)). Pristine SA-TCPP shows a broad band at 2500–3300 cm^{-1} attributed to O–H and N–H stretching vibrations, and characteristic peaks at 1602 and 1402 cm^{-1} corresponding to the C=C and C=N vibrations of the porphyrin ring, respectively. NH_2-PDMS exhibits typical C–H stretching bands at 2962 and 2902 cm^{-1} and Si–C vibration bands at 862 and 786 cm^{-1}. All these characteristic peaks are retained in the NH_2-PDMS@SA-TCPP spectrum, confirming the coexistence of SA-TCPP and NH_2-PDMS in the NH_2-PDMS@SA-TCPP catalyst. Importantly, the C=O stretching band of SA-TCPP shows a slight blue shift from 1687 to 1675 cm^{-1} [26–28], indicating that amide bonds may form between the carboxyl groups of SA-TCPP and the amino groups of PDMS in the NH_2-PDMS@SA-TCPP catalyst.

The ^{13}C nuclear magnetic resonance (NMR) spectrum further confirms this interaction (Fig. 2(b)), the ^{13}C NMR spectrum of pristine SA-TCPP displays characteristic signals at 167.9, 145.9, 134.9, 130.9, 128.4, and 119.8 ppm, corresponding to the porphyrin framework [20]. After NH_2-PDMS modification, these signals are largely retained, indicating that the conjugated skeleton remains intact. Importantly, a new resonance peak emerges at 173.8 ppm, which is downfield relative to the carboxyl carbon at 167.9 ppm [29, 30]. This downfield shift is characteristic of an amide carbonyl, further suggesting that amide bonds form between SA-TCPP and NH_2-PDMS.

The formation of amide bonds between SA-TCPP and NH_2-PDMS was further confirmed by X-ray photoelectron spectroscopy (XPS). As shown in Fig. 2(c), the C 1s spectrum of pristine SA-TCPP exhibits three characteristic peaks at 284.8 eV (C–C/C–H), 285.8 eV (C–O/C–N), and 289.0 eV (O–C=O), corresponding to the porphyrin skeleton and terminal carboxyl groups [20, 31, 32]. After NH_2-PDMS modification, the intensity of the O–C=O signal markedly decreases, accompanied by the emergence of new peaks at ~ 286.8 and 283.8 eV, which are assigned to amide (–CONH–) and C–Si bonds, respectively, indicating partial conversion of –COOH to –CONH– functionalities. The O 1s spectrum (Fig. 2(d)) also reveals a shift of the carbonyl-related component from 529.8 to 530.6 eV due to the formation of electron-deficient amide carbonyls, along with a Si–O–Si feature at 528.7 eV. Furthermore, the N 1s (Fig. S5(a) in the ESM) and Si 2p spectra (Fig. S5(b) in the ESM) display characteristic peaks corresponding to N–C=O (397.2 eV), Si–C (102.1 eV), and Si–O–Si (102.7 eV) bonds [33, 34]. These findings, together with the FTIR and ^{13}C NMR analyses, provide compelling evidence that NH_2-PDMS is covalently grafted onto the porphyrin framework through amide bond formation.

Meanwhile, the thermogravimetric (TG)/differential thermal analysis (DTA) of NH_2-PDMS@SA-TCPP retains the thermal decomposition characteristics of SA-TCPP while the additional mass loss originates from NH_2-PDMS, indicating that its incorporation enhances thermal stability without affecting the porphyrin framework (Fig. S6 in the ESM).

Figure 3(a) shows the ultraviolet–visible–near-infrared (UV–Vis–NIR) diffuse reflectance spectra (DRS) of the NH_2-

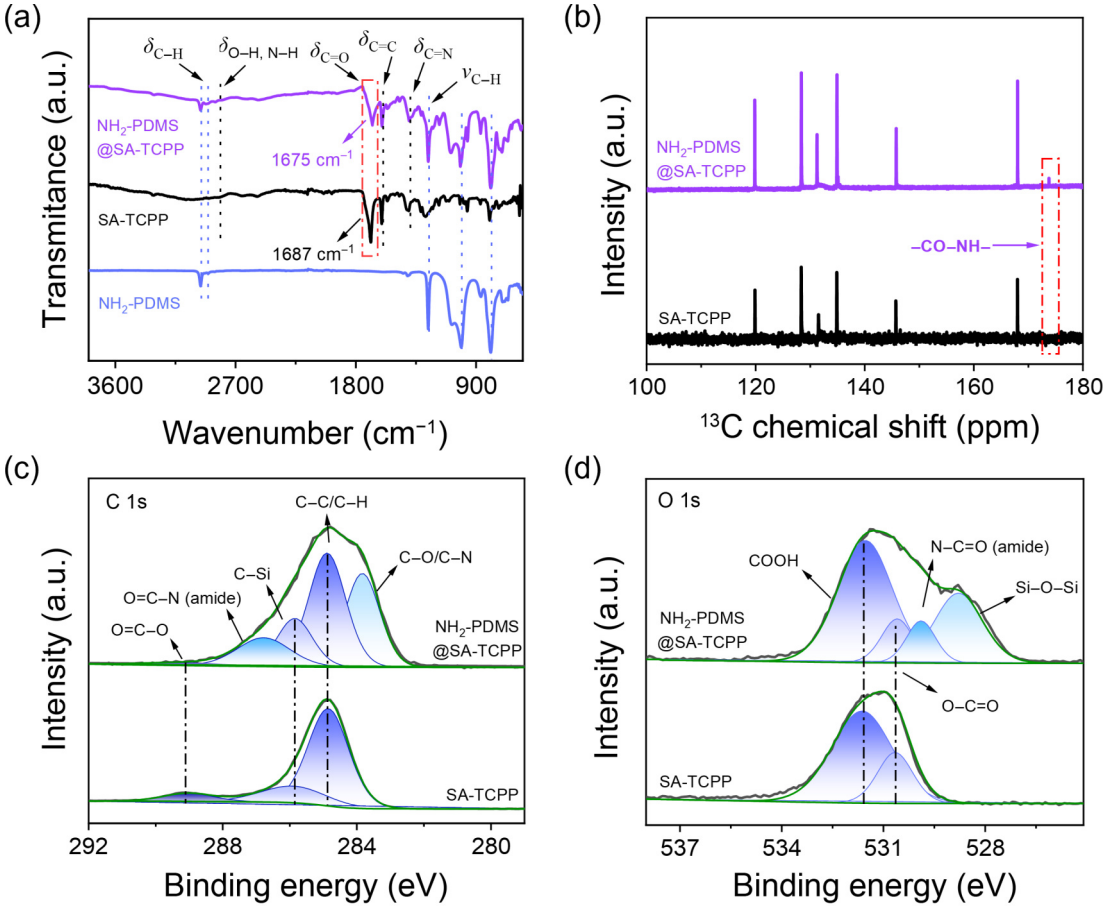

Figure 2 (a) FTIR spectra of NH_2-PDMS, SA-TCPP and NH_2-PDMS@SA-TCPP catalysts. (b) Comparison of ^{13}C NMR spectra of SA-TCPP and NH_2-PDMS@SA-TCPP. (c) C 1s and (d) O 1s XPS spectra of SA-TCPP and NH_2-PDMS@SA-TCPP catalysts.

PDMS@SA-TCPP catalyst, with pristine SA-TCPP supramolecules as a reference. Both samples exhibit a pronounced Soret band at 415–430 nm and a broad absorption tail extending to about 1100 nm, reflecting their narrow bandgap characteristics. The nearly identical absorption edges and intensities indicate that the incorporation of NH_2-PDMS does not affect the intrinsic light-harvesting capability and electronic structure of the porphyrin framework. Based on the Kubelka–Munk function (Fig. 3(b)), the optical bandgap of NH_2-PDMS@SA-TCPP catalyst is estimated to be 1.65 eV. The band structure of NH_2-PDMS@SA-TCPP is further investigated using Mott–Schottky analysis (Fig. 3(c)). The linear region of the Mott–Schottky plot reveals a flat-band potential (E_{fb}) of −0.12 V vs. Ag/AgCl, which corresponds to the Fermi level of the n-type TCPP semiconductor. Using the relation $E_{CB} = E_{fb} - X$ (with X = 0.1 V for TCPP) and an optical band gap of 1.65 eV, the conduction and valence band edges are −0.01 and 1.64 V vs. RHE, respectively. Moreover, the valence band energy (E_{VB}) obtained from the XPS valence-band spectrum (Fig. S7 in the ESM) is 1.64 V, which shows excellent agreement with the result derived from the Mott–Schottky analysis. As illustrated in Fig. 3(d), the schematic energy-band diagram clearly shows that the band positions of NH_2-PDMS@SA-TCPP catalyst remain nearly identical to those of SA-TCPP catalyst. Therefore, NH_2-PDMS@SA-TCPP catalyst possess conduction bands sufficiently negative to drive the O_2/H_2O_2 redox reaction (0.68 V vs. RHE) and valence bands positive enough to promote the ROOOH/ROOH oxidation process (1.51 V vs. RHE), consistent with the dual-pathway mechanism previously demonstrated by our group, in which O_2 undergoes reductions on the NH group in the porphyrin ring, while photogenerated holes oxidize peripheral carboxyl groups (–COOH) to percarboxylic acids (–COOOH) that further hydrolyze to H_2O_2. The NH_2-PDMS modification preserves the fundamental electronic configuration and photocatalytic reaction pathway responsible for efficient H_2O_2 generation.

3.2 Dispersion of NH_2-PDMS@SA-TCPP in the biphasic system

To function effectively in a water/n-decane biphasic system, the SA-TCPP catalyst may possess sufficient hydrophobicity. Pristine SA-TCPP, rich in carboxyl groups, exhibits a low water contact angle of only 50° (Fig. 4(a)), indicating substantial hydrophilicity. By introducing amino-terminated polydimethylsiloxane (NH_2-PDMS) as a hydrophobic anchoring modifier and chemically grafting siloxane chains onto the SA-TCPP framework, the surface of SA-TCPP is successfully modified. After modification, the water contact angle of NH_2-PDMS@SA-TCPP increases markedly to 136°, confirming the successful transformation of the catalyst from hydrophilic to strongly hydrophobic. Therefore, in a water/hydrophobic organic solvent system (n-decane, Fig. 4(b)), the pristine SA-TCPP tends to disperse in the lower aqueous phase. In contrast, NH_2-PDMS@SA-TCPP disperses in the upper organic phase, thereby achieving clear spatial separation from the aqueous phase. Dynamic light scattering (DLS) analysis shows that NH_2-PDMS@SA-TCPP forms uniform nanosheets in n-decane, with an

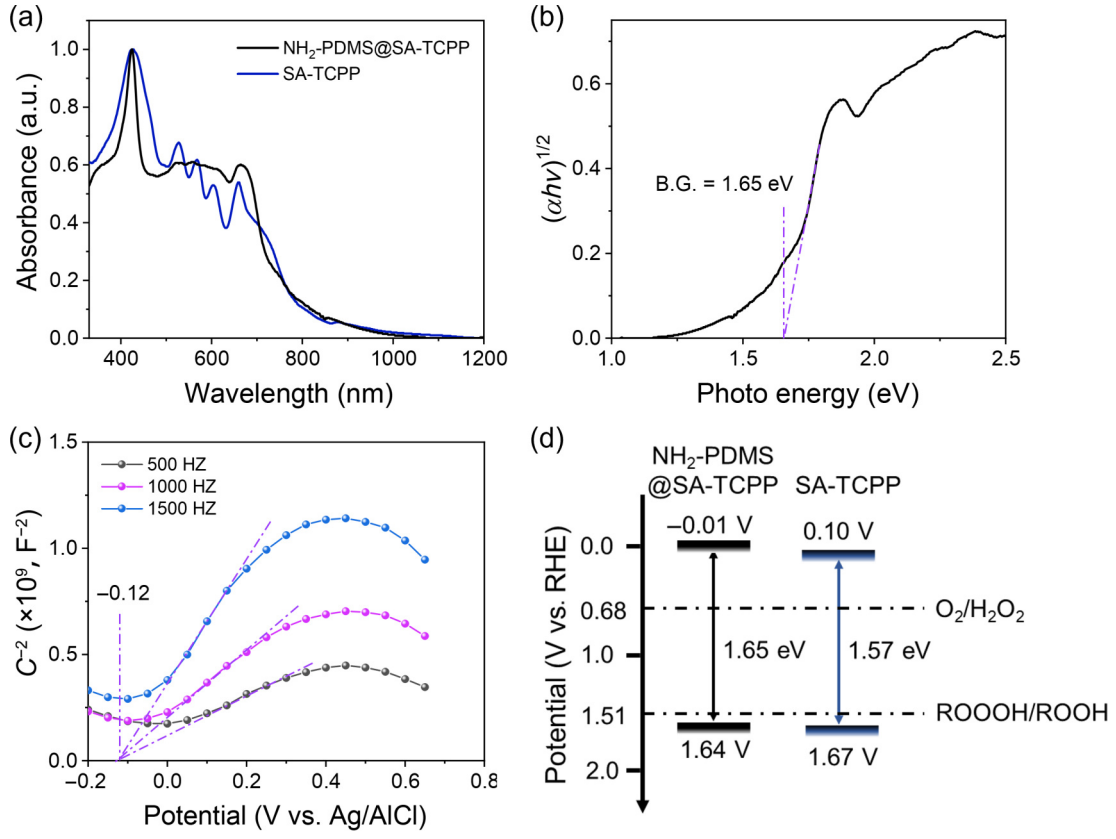

Figure 3 (a) UV–Vis–NIR DRS of the NH_2-PDMS@SA-TCPP and SA-TCPP catalysts. (b) Tauc plot ($(\alpha h\nu)^{1/2}$ vs. $h\nu$) of the NH_2-PDMS@SA-TCPP catalyst, where α, h, and ν represent the absorption coefficient, Planck's constant, and light frequency, respectively. The intersection of the extrapolated tangent and baseline corresponds to the band gap (BG). (c) Mott–Schottky plots of the NH_2-PDMS@SA-TCPP catalyst. The flat-band potential (E_{fb}) is determined from the x-intercept of the linear portion of the Mott–Schottky plots. (d) Schematic illustration of the band edge positions of the NH_2-PDMS@SA-TCPP and SA-TCPP catalysts.

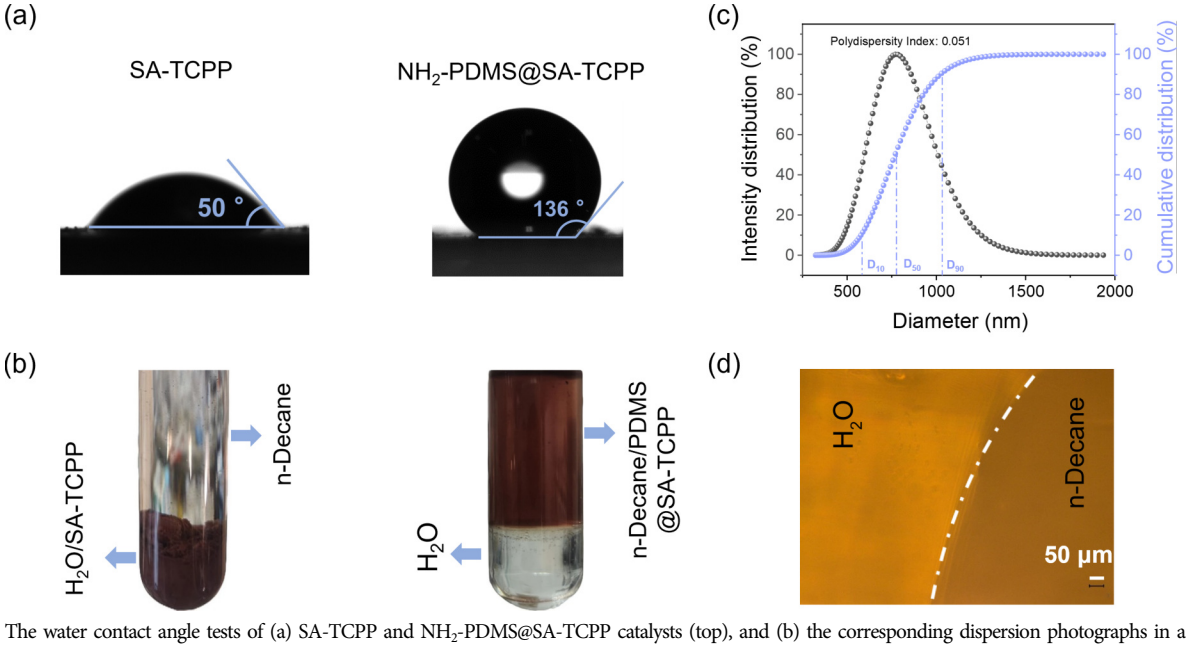

Figure 4 The water contact angle tests of (a) SA-TCPP and NH_2-PDMS@SA-TCPP catalysts (top), and (b) the corresponding dispersion photographs in a water/n-decane biphasic system (bottom). (c) Particle size distribution of NH_2-PDMS@SA-TCPP catalyst in n-decane by DLS. Black: intensity distribution; blue: cumulative distribution. (d) Optical microscopy image of the phase interface between water and n-decane.

average diameter of ~ 775 nm and a low polydispersity index (PDI = 0.051), indicating excellent dispersibility of NH_2-PDMS@SA-TCPP within the organic phase (Fig. 4(c)). To more closely examine the NH_2-PDMS@SA-TCPP catalyst distribution, the aqueous phase is stained with potassium titanium oxalate and H_2O_2 and is observed under an optical microscope (Fig. 4(d)). The organic phase, although inherently colorless, appears distinctly darker than the aqueous phase, indicating that the NH_2-PDMS@SA-

TCPP catalyst is primarily localized in the organic phase. A clearly curved interface is also observed, resulting from the significant interfacial tension difference (51.4 mN·m^{-1}) between the aqueous and organic phases [35]. In addition, UV–Vis spectroscopy confirms that the NH_2-PDMS@SA-TCPP catalyst is almost completely confined to the organic phase, as the characteristic absorbance of NH_2-PDMS@SA-TCPP in the aqueous phase is nearly negligible (Fig. S8 in the ESM).

These findings indicate that the NH_2-PDMS@SA-TCPP catalyst disperses exclusively in the organic phase, enabling efficient spatial separation between the photocatalyst and the produced H_2O_2, which in turn facilitates the continuous formation and enrichment of H_2O_2 in the aqueous phase.

3.3 Photocatalytic H_2O_2 production on the NH_2-PDMS@SA-TCPP in the biphasic system

The photocatalytic H_2O_2 production of the NH_2-PDMS@SA-TCPP catalyst was evaluated under visible-light irradiation for 4 h, using SA-TCPP and the monophasic aqueous system as controls (Fig. 5(a)). In the biphasic system, NH_2-PDMS@SA-TCPP achieves a maximum H_2O_2 concentration of 42 mM, compared to only 15 mM for SA-TCPP, corresponding to an approximately three times higher yield. Notably, NH_2-PDMS itself exhibits no detectable photocatalytic activity toward H_2O_2 generation (Fig. S9 in the ESM). Further comparison with the aqueous system shows that the H_2O_2 concentration of NH_2-PDMS@SA-TCPP under biphasic conditions is 19 times higher than that in pure water (42 mM vs. 2 mM), in addition, less than 0.48% of the generated H_2O_2 is detected in the n-decane phase based on aqueous extraction (Fig. S10 in the ESM). This result indicates that NH_2-PDMS@SA-TCPP exhibits much higher reaction efficiency in the presence of an n-decane inert organic phase. The chemical stability of n-decane before and after the photocatalytic reaction is examined by ^{1}H NMR spectroscopy, and no chemical changes are observed (Fig. S11 in the ESM).

Benefiting from the stable biphasic reaction environment, NH_2-PDMS@SA-TCPP maintains approximately 90% of its catalytic activity after five consecutive cycles under visible-light irradiation (Fig. 5(b)). The structural integrity of the NH_2-PDMS@SA-TCPP catalyst is well preserved after cycling, as confirmed by FTIR analysis (Fig. S12 in the ESM). After 12 h of reaction, the H_2O_2 accumulates and concentrates to 0.65 wt.%, approaching the level required for practical aqueous applications, indicating that the biphasic photocatalytic strategy effectively enables *in situ* enrichment of dispersed H_2O_2 (Figs. S13 and S14 in the ESM). Moreover, no n-decane is detected in the aqueous phase after the reaction (Fig. S15 in the ESM), which enables the direct collection of the aqueous H_2O_2 product without purification.

As shown in Fig. 5(c), the apparent quantum efficiency (AQE) of

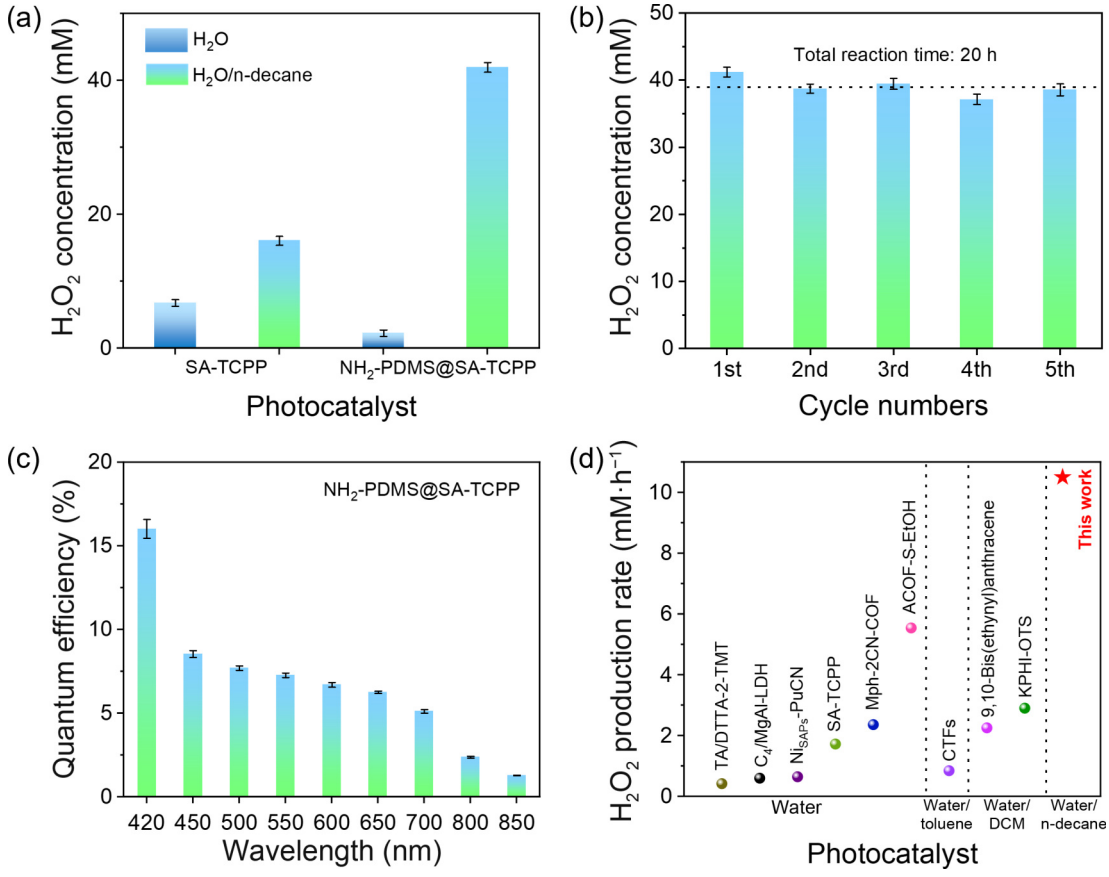

Figure 5 (a) Comparison of H_2O_2 production by pristine SA-TCPP and the NH_2-PDMS@SA-TCPP catalysts in an aqueous phase and a water/n-decane biphasic system. (b) Cycle stability of the NH_2-PDMS@SA-TCPP catalyst over 5 repeated runs. (c) AQE of the NH_2-PDMS@SA-TCPP measured with different band-pass filters (420 ± 10, 450 ± 10, 500 ± 10, 550 ± 10, 600 ± 10, 650 ± 10, 700 ± 10, 800 ± 10, and 850 ± 10 nm). (d) Comparison of H_2O_2 production by NH_2-PDMS@SA-TCPP in water/organic biphasic system and inert organic phases, as well as reference systems employing highly active catalysts in the aqueous phase. Reaction conditions: solution volume, 30 mL (water:n-decane = 1:5), reaction temperature: 80 °C, NH_2-PDMS@SA-TCPP catalyst: 45 mg, O_2 bubbling, reaction time: 4 h, light source: Xe lamp with a 420 nm cut-off filter.

the NH_2-PDMS@SA-TCPP catalyst is measured as a function of incident wavelength using band-pass filters in the range of 420 ± 10 to 850 ± 10 nm. The AQE reaches a maximum of 16.02% at 420 ± 10 nm, compared with other top-performing photocatalysts in aqueous systems (ca. 15.80% at 400 nm) [36–41], and gradually decreases at longer wavelengths, which is consistent with the absorption characteristics of NH_2-PDMS@SA-TCPP (Fig. 3(a)). Notably, a detectable response is still observed beyond 850 ± 10 nm, indicating the effective utilization of both visible and near-infrared light. Correspondingly, the NH_2-PDMS@SA-TCPP catalyst exhibits an H_2O_2 generation rate of 10.5 $mM \cdot h^{-1}$. which surpasses most previously reported photocatalytic systems operated in aqueous and water/inert organic biphasic (Fig. 5(d)).

Compared with water, n-decane exhibits a substantially higher oxygen solubility. Based on an anthracene fluorescence quenching evaluation [42, 43], the dissolved oxygen concentration in n-decane decreases from 61.7 mM at 20 °C to 13.3 mM at 80 °C, which is about 51 times higher than that in water at 20 °C (ca. 1.2 mM) (Fig. S16 in the ESM). However, despite the higher oxygen solubility at lower temperatures, the H_2O_2 generation rate does not reach its maximum under these conditions, indicating that temperature-dependent reaction kinetics play a more dominant role than oxygen availability.

In our previous study, we demonstrated that H_2O_2 generation proceeds through two pathways,namely, the reduction of O_2 and the hole-driven oxidation of carboxyl groups to percarboxylic acids. Temperature serves as a critical parameter governing the generated peroxyl-group intermediates to hydrolyze and regenerated COOH groups and H_2O_2, as higher temperatures promote the hydrolysis of peroxy acid. The accelerated hydrolysis suppresses the accumulation of peroxyacid species (i.e., recombination centers), thereby enhancing the overall efficiency of H_2O_2 production. Therefore, we investigate the activity of the NH_2-PDMS@SA-TCPP catalyst for H_2O_2 production at different reaction temperatures. As the temperature increases from 60 to 80 °C, the H_2O_2 concentration gradually rises, reaching a maximum value of 42 mM at 80 °C (Fig. 6(a)). However, further increasing the temperature to 90 °C leads to a pronounced decline in activity due to the decomposition of high concentrated H_2O_2.

The effect of the aqueous phase on photocatalytic H_2O_2 production was systematically investigated by varying the water-to-organic phase ratio from 20:10 to 2:28 (v/v) (Fig. 6(b)). The H_2O_2 concentration increases significantly from 8 to 45 mM, whereas the total amount of H_2O_2 generated first increases at moderate ratios (20:10–5:25) and then decreases sharply at the lowest ratio (2:28). This observation indicates that the increase in concentration does not correspond to a proportional increase in total H_2O_2 yield. The reason probably lies in the dispersion state of the NH_2-PDMS@SA-TCPP catalyst in the biphasic system. NH_2-PDMS@SA-TCPP is mainly dispersed in the organic phase (Fig. 4(d)), while the aqueous

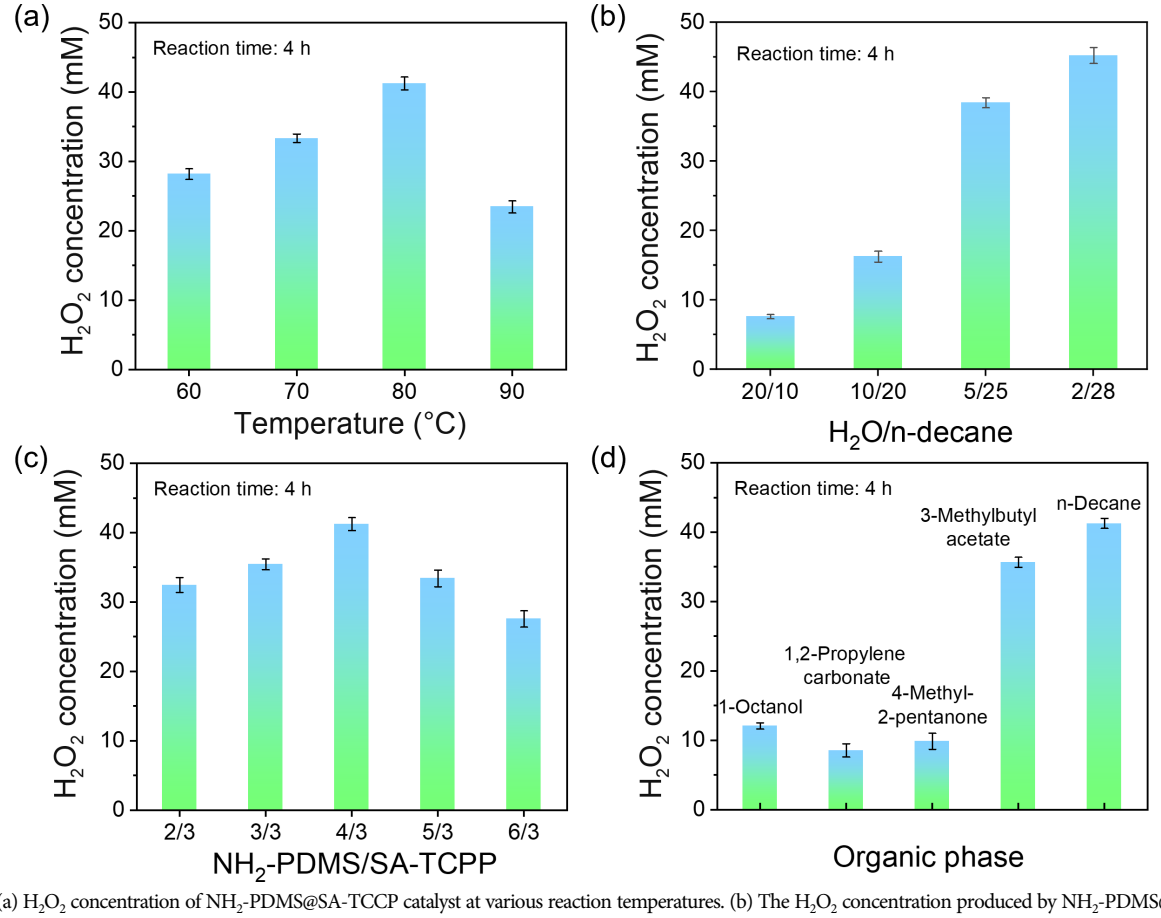

Figure 6 (a) H_2O_2 concentration of NH_2-PDMS@SA-TCCP catalyst at various reaction temperatures. (b) The H_2O_2 concentration produced by NH_2-PDMS@SA-TCPP catalyst in different water/n-decane volume ratios. (c) The H_2O_2 concentration produced by NH_2-PDMS@SA-TCPP catalyst in different NH_2-PDMS to SA-TCPP mass ratios. (d) H_2O_2 production of the NH_2-PDMS@SA-TCPP in water/organic biphasic systems using different organic phases (e.g., 1-octanol, 1,2-propylene carbonate, 4-methyl-2-pentanone, 3-methylbutyl acetate, n-decane). Reaction conditions: solution volume, 30 mL (water:n-decane = 1:5), reaction temperature: 80 °C, NH_2-PDMS@SA-TCPP catalyst: 45 mg, O_2 bubbling, reaction time: 4 h, light source: Xe lamp with a 420 nm cut-off filter.

phase provides the environment for H_2O_2 generation and diffusion. As the aqueous volume increases, the content of the organic phase decreases, leading to poorer dispersion of the NH_2-PDMS@SA-TCPP catalyst with the same mass, and particle aggregation occurs (Fig. S17(a) in the ESM), resulting in a lower H_2O_2 concentration in the aqueous phase. When the aqueous volume is decreased, the NH_2-PDMS@SA-TCPP catalyst disperses more uniformly (Fig. S17(b) in the ESM), and the produced H_2O_2 concentration increases significantly. However, the higher H_2O_2 concentration also accelerates its decomposition. Considering both the H_2O_2 concentration and total yield, the optimal water-to-organic phase ratio is 5 mL/25 mL.

Building upon the investigation of the water-to-organic phase volume ratio, we further examined the effect of the NH_2-PDMS/SA-TCPP mass ratio (2:3–6:3) on photocatalytic H_2O_2 production in the biphasic system (Fig. 6(c)). As shown in Fig. 6(c), the H_2O_2 concentration first increases and then decreases with increasing NH_2-PDMS content, reaching a maximum of 42 mM at the 4:3 ratio. At lower NH_2-PDMS content, the NH_2-PDMS@SA-TCPP catalyst exhibits partial dispersion in the aqueous phase. The ^{13}C NMR spectrum of the aqueous-phase catalyst (Fig. S18 in the ESM) shows no characteristic signals of amide bond formation, indicating that insufficient amide coupling between NH_2-PDMS and SA-TCPP leads to incomplete surface modification and consequently reduces the H_2O_2 activity. In contrast, excessive NH_2-PDMS (≥ 5:3) may encapsulate the SA-TCPP catalyst, thereby reducing the accessibility of active sites. Moreover, a high NH_2-PDMS content leads to aggregation of the SA-TCPP, further decreasing the dispersion of NH_2-PDMS@SA-TCPP catalyst (Fig. S19 in the ESM). These results highlight that a moderate amount of NH_2-PDMS is essential to balance surface modification and oxygen transport, with the 4:3 ratio representing the optimal condition for maximizing H_2O_2 production.

To further verify the general applicability of biphasic system, representative organic solvents with different polarities were examined, including protic polar (e.g., 1-octanol), aprotic polar (e.g., 1,2-propylene carbonate), medium-polar (e.g., 4-methyl-2-pentanone), low-polar (e.g., 3-methylbutyl acetate), and nonpolar (n-decane) solvents (Fig. 6(d)). When 1-octanol and 1,2-propylene carbonate are used as the organic phases, the H_2O_2 concentrations are 12.0 and 8.5 mM, respectively. The slightly higher activity in the 1-octanol-based system is attributed to its protic nature, which allows it to act as a mild hole scavenger. To reliably evaluate the intrinsic photocatalytic performance of the NH_2-PDMS@SA-TCPP catalyst, non-sacrificial organic phases are therefore employed in subsequent experiments. As the solvent polarity decreases (1,2-propylene carbonate > 4-methyl-2-pentanone > 3-methylbutyl acetate > n-decane), the H_2O_2 concentration gradually increases from 8.5 to 42 mM, with NH_2-PDMS@SA-TCPP exhibiting the highest activity in the water/n-decane system. In polar solvents, porphyrin molecules tend to dissolve, disrupting their supramolecular assemblies (Fig. S20 in the ESM).

In contrast, nonpolar solvents preserve the structural integrity of NH_2-PDMS@SA-TCPP catalyst. As show from Fig. S21 in the ESM, similar results are observed with solvents of comparable nonpolar, such as toluene, n-heptane and n-dodecane, which exhibit consistent H_2O_2 concentrations with n-decane, further confirming the general effectiveness of NH_2-PDMS@SA-TCPP biphasic photocatalytic system across different nonpolar organic-water combinations.

Taken together, these results indicate that careful adjustment of reaction parameters, including reaction temperature, water/organic phase volume ratio, NH_2-PDMS/SA-TCPP mass ratio, and organic solvent polarity, is essential, as adequate dispersion of the NH_2-PDMS@SA-TCPP catalyst within the organic phase is the key factor for achieving high photocatalytic H_2O_2 production.

3.4 Mechanism of NH_2-PDMS@SA-TCPP in biphasic system

To gain deeper insight into the microenvironment of H_2O_2 formation, the behavior of the NH_2-PDMS@SA-TCPP catalyst was investigated in a sole-n-decane system, where no external water is introduced, and the trace moisture originated solely from the solvent itself. *In situ* FTIR spectroscopy of NH_2-PDMS@SA-TCPP dispersed in pure n-decane under visible-light irradiation exhibits several characteristic absorption bands (Fig. 7(a)). The characteristic absorption bands at 838 cm^{-1} [44, 45] and 1282 cm^{-1} [46, 47] correspond to O–O stretching and peroxide-related vibrations, respectively, providing direct evidence for oxygen reduction and peroxide formation in the hydrophobic organic phase. Moreover, the broad peak around 3240 cm^{-1} (O–H stretching) [48] confirms the formation of H_2O_2 molecules. This observation is further supported by the EPR spectra of NH_2-PDMS@SA-TCPP in the pure organic phase (Fig. 7(b)). Furthermore, the H_2O_2 formed in pure n-decane is successfully extracted into the aqueous phase and verified by a horseradish peroxidase (HRP)-coupled photoluminescence (PL) assay (Fig. S22 in the ESM). Together with the *in situ* FTIR and EPR results, these findings confirm that the NH_2-PDMS@SA-TCPP catalyst directly generates H_2O_2 in the organic phase.

To further elucidate the hole oxidation pathway, the post-reaction structure of NH_2-PDMS@SA-TCPP in pure n-decane was characterized by ^{13}C NMR spectroscopy (Fig. 7(c)) and compared with that before the reaction. Prominent ^{13}C NMR signals at 166.1, 140.3, 128.9, 128.5, and 118.3 ppm are observed, corresponding to –COOOH groups formed via the oxidation of –COOH, consistent with our previous report. Meanwhile, the characteristic peaks of the amide carbonyl group remain unchanged, further confirming that the amide linkage between NH_2-PDMS and SA-TCPP is preserved after the reaction. The results indicate that, in the organic phase, H_2O_2 is generated not only through O_2 reduction but also through the photogenerated-hole-driven oxidation of porphyrin carboxyl groups, forming peroxycarboxylic acid intermediates that are subsequently hydrolyzed to produce H_2O_2 [20].

To more intuitively understand the accumulation mechanism of H_2O_2 in the aqueous phase of the biphasic system, NH_2-PDMS@SA-TCPP is dispersed in the organic phase above water and irradiated with visible light under static conditions. The H_2O_2 concentration in the underlying aqueous phase is monitored using PL. As shown in Fig. 7(d), the PL intensity gradually increases over time, reflecting the continuous migration and progressive accumulation of H_2O_2 from the organic phase into the aqueous phase. This time-dependent enhancement highlights the mass transfer and effective enrichment of H_2O_2 in the aqueous phase.

Under stirred conditions, the aqueous phase does not exist as a continuous layer, but rather as fine water droplets dispersed around the NH_2-PDMS@SA-TCPP catalyst particles (Fig. 7(e)). These microdroplets create a dynamic microenvironment that enables efficient extraction of the hydrophilic H_2O_2 molecules immediately after their formation. Once H_2O_2 is generated on the NH_2-

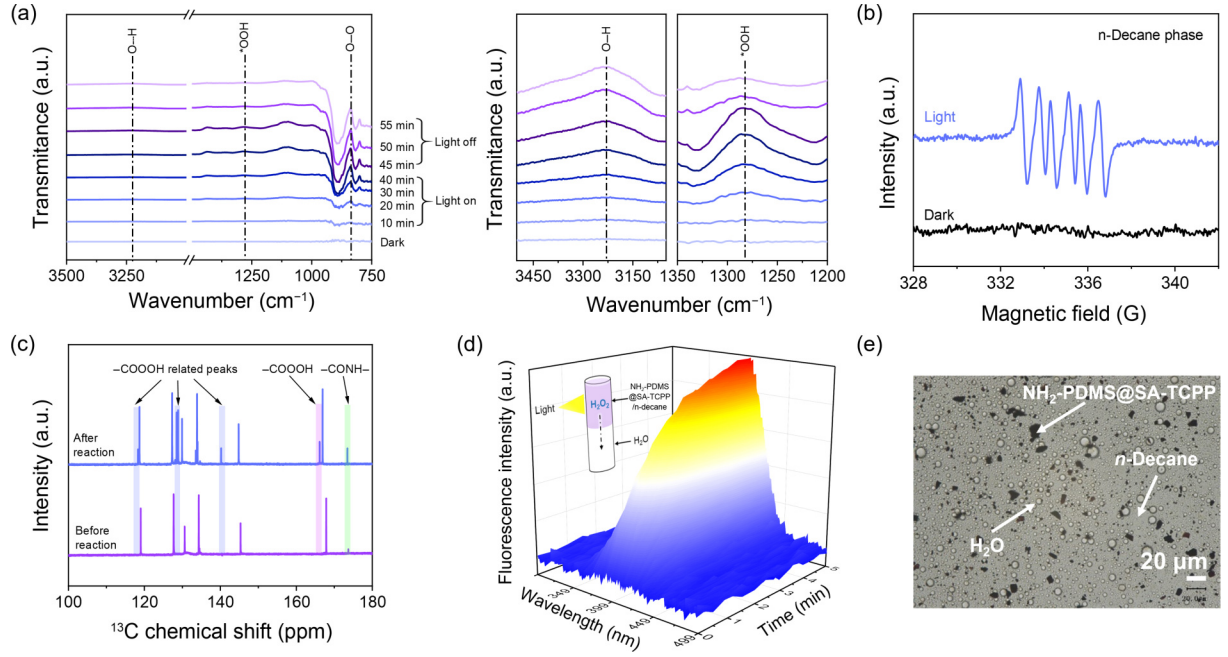

Figure 7 (a) *In situ* FTIR spectra of the NH_2-PDMS@SA-TCPP catalyst in the pure n-decane phase and the corresponding magnified region. (b) EPR spectra of superoxide radicals (O_2^-) produced by the NH_2-PDMS@SA-TCPP catalyst in the pure n-decane phase. (c) ^{13}C NMR spectrum of the NH_2-PDMS@SA-TCPP catalyst after the photocatalytic reaction in the n-decane phase. (d) Time-resolved three-dimensional (3D) PL spectra of aqueous-phase H_2O_2 detected by HRP under visible-light irradiation, where the NH_2-PDMS@SA-TCPP catalyst is dispersed in the organic phase (static system). Inset: Schematic illustration of the reaction setup. (e) Optical microscopy image of the NH_2-PDMS@SA-TCPP catalyst dispersed in a biphasic (water/n-decane) system.

PDMS@SA-TCPP catalyst surface, it rapidly migrates from the organic phase into the surrounding water microdomains due to its high solubility, effectively detaching from the catalytic sites. The rapid removal of H_2O_2 minimizes secondary decomposition reactions and helps maintain the structural integrity of the NH_2-PDMS@SA-TCPP catalyst during continuous operation (Fig. S23 in the ESM).

At the same time, n-decane provides an oxygen-rich environment. This abundant oxygen supply greatly accelerates the reduction reaction rate and enhances the overall H_2O_2 generation efficiency. Therefore, the n-decane phase serves as a favorable medium for rapid photocatalytic oxygen reduction, while the dispersed aqueous phase acts as an efficient reservoir for H_2O_2 storage and stabilization. The synergistic cooperation between these two phases simultaneously enhances both H_2O_2 formation and concentration (Fig. 8).

4 Conclusions

In summary, this study develops a water/n-decane biphasic photocatalytic H_2O_2 production system, employing an amino-functionalized polydimethylsiloxane-modified supramolecular porphyrin (NH_2-PDMS@SA-TCPP) as the photocatalyst. The incorporation of NH_2-PDMS forms amide linkages (–CO–NH–) with SA-TCPP, rendering the NH_2-PDMS@SA-TCPP catalyst hydrophobic and promoting its preferential dispersion in the organic phase. Under visible-light irradiation, H_2O_2 is demonstrated to mainly generate in the organic n-decane phase and subsequently transfer and concentrate in the aqueous phase, which effectively mitigates H_2O_2 decomposition and enhances H_2O_2 accumulation. The developed system achieves a generation rate of 10.5 mM·h^{-1}, and an apparent quantum efficiency as high as 16.02% at 420 nm. This work demonstrates that tuning the surface hydrophobicity of porphyrin-based catalysts regulates H_2O_2 distribution and stability, providing a practical strategy for designing efficient, recyclable, and scalable biphasic photocatalytic systems for sustainable H_2O_2 production in the future.

Electronic Supplementary Material: Supplementary material (SEM and TEM images; XRD patterns; XPS spectra; GPC curves; TG–DTA curves; UV–Vis absorption spectra; ^1H and ^{13}C NMR spectra; FTIR spectra; PL and time-resolved PL decay spectra; and rheological measurements) is available in the online version of this article at https://doi.org/10.26599/NR.2026.94908474.

Data availability

All data needed to support the conclusions in the paper are presented in the manuscript and the Electronic Supplementary Material. Additional data related to this paper may be requested from the corresponding author upon request.

Acknowledgements

This research is supported by the National Natural Science Foundation of China (Nos. 22172065 and 22476071), Natural Science Foundation of Hebei Province (No. E2024210028), the Postgraduate Research and Practice Innovation Program of Jiangsu Province (No. KYCX24_2532), and the Fundamental Research Funds for the Central Universities. The authors also thank the Central Laboratory, School of Chemical and Material Engineering, Jiangnan University.

Declaration of competing interest

All the contributing authors declare no conflict of interests in this work.

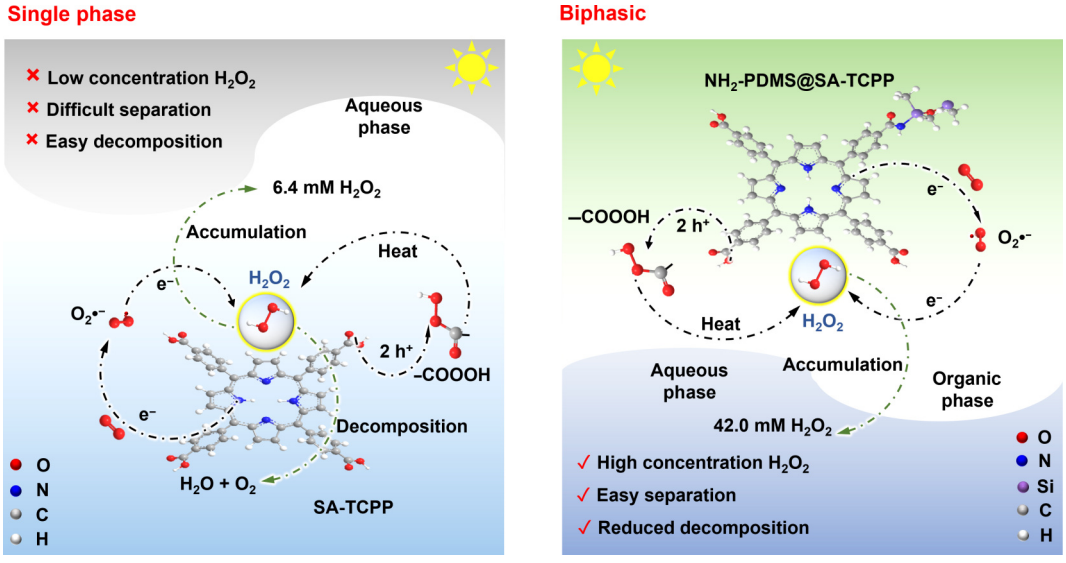

Figure 8 Schematic illustration of photocatalytic H_2O_2 production in single phase and biphasic systems.

Author contribution statement

J. L. carried out the investigation, visualization, and drafted the original manuscript. H. J. S. contributed to manuscript editing, validation and investigation. W. T. Q. conducted the SEM. S. D. performed the AQE analysis. Y. N. Z. conducted the FTIR measurements. J. X., J. W. Z., Y. Z., and Y. L. participated in data analysis and manuscript discussions. Y. F. Z. contributed to manuscript review and supervision. C. S. P. conceived the research idea, contributed to the conceptualization and methodology, oversaw writing – review & editing, provided resources, and supervised the project. All authors discussed the results, revised the manuscript, and approved the final version.

Use of AI statement

None.

References

[1] Kim, H. I.; Choi, Y.; Hu, S.; Choi, W.; Kim, J. H. Photocatalytic hydrogen peroxide production by anthraquinone-augmented polymeric carbon nitride. *Appl. Catal. B: Environ.* **2018**, *229*, 121–129.

[2] Yan, S. W.; Li, Y.; Yang, X. Y.; Jia, X. H.; Xu, J. S.; Song, H. J. Photocatalytic H_2O_2 generation reaction with a benchmark rate at air-liquid-solid joint interfaces. *Adv. Mater.* **2024**, *36*, 2307967.

[3] Bao, C. H.; Li, L.; Wang, X. F.; Xia, S. S.; Wang, X. S.; Jin, C. C.; Chen, Z. Bringing porous framework materials toward photocatalytic H_2O_2 production. *Nano Lett.* **2025**, *25*, 4115–4136.

[4] Li, Y. X.; Pei, Z. H.; Luan, D. Y.; Lou, X. W. D. Triple-phase photocatalytic H_2O_2 production on a Janus fiber membrane with asymmetric hydrophobicity. *J. Am. Chem. Soc.* **2024**, *146*, 3343–3351.

[5] Yu, Z. Y.; Li, S. C.; Wu, Y. F.; Ma, C. F.; Li, J. N.; Duan, L. Y.; Liu, Z. C.; Sun, H. N.; Zhao, G. F.; Lu, Y. et al. Continuous photocatalytic preparation of hydrogen peroxide with anthraquinone photosensitizers. *Green Chem.* **2024**, *26*, 9310–9319.

[6] Wang, L.; Fang, C. Y.; Xu, B. R.; Yu, Y. L.; Liu, Y. M.; Fu, X. B.; Cao, A.; Sun, Q. Q.; Zhou S. B. A ZnO-based catalytic system for the synthesis of hydrogen peroxide from air. *Angew. Chem., Int. Ed.* **2025**, *64*, e202424984.

[7] Kondo, Y.; Kuwahara, Y.; Mori, K.; Yamashita, H. Design of metal-organic framework catalysts for photocatalytic hydrogen peroxide production. *Chem.* **2022**, *8*, 2924–2938.

[8] Li, L.; Wang, X. F.; Bao, C. H.; Cai, Y. X.; Ding, K. X.; Wang, X. S.; Sun, J.; Jin, C. C.; Chen, Z. In-depth insight into variable connected zirconium porphyrin metal-organic frameworks for H_2O_2 photosynthesis in pure water. *Appl. Catal. A: Gen.* **2026**, *709*, 120647.

[9] Xia, S. S.; Li, L.; Bao, C. H.; Wu, J. H.; Li, C. Y.; Wang, X. Z.; Gao, J. Y.; Hu, J. L.; Wang, X. S.; Chen, Z. Photosynthesis of H_2O_2 in pure water over 2D metal-organic frameworks film by co-doping Ga and porphyrin. *J. Catal.* **2024**, *433*, 115488.

[10] Li, C. Y.; Cai, Y. X.; Wu, J. H.; Li, L.; Xia, S. S.; Wang, X. Z.; Jia, R. R.; Chen, Z.; Jin, C. C.; Wang, W. et al. High-concentration single-atom Zn-doped porous tubular g-C_3N_4: A superior photocatalyst for tetracycline hydrochloride degradation and bacterial sterilization. *Rare Met.* **2025**, *44*, 4756–4766.

[11] Yang, X. R.; Chen, Z.; Zhao, W.; Liu, C. X.; Qian, X. X.; Zhang, M.; Wei, G. Y.; Khan, E.; Hau Ng, Y.; Ok, Y. S. Recent advances in photodegradation of antibiotic residues in water. *Chem. Eng. J.* **2021**, *405*, 126806.

[12] Zhou, L.; Lei, J. Y.; Wang, F. C.; Wang, L. Z.; Hoffmann, M. R.; Liu, Y. D.; In, S. I.; Zhang, J. L. Carbon nitride nanotubes with *in situ* grafted hydroxyl groups for highly efficient spontaneous H_2O_2 production. *Appl. Catal. B: Environ.* **2021**, *288*, 119993.

[13] Shao, Y. H.; Zhang, Y. N.; Chen, C. F.; Dou, S.; Lou, Y.; Dong, Y. M.; Zhu, Y. F.; Pan, C. S. Enhancement of H_2O_2 generation rate in porphyrin photocatalysts via crystal facets regulation to create strong internal electric field. *Chin. J. Catal.* **2024**, *61*, 205–214.

[14] Prabhavathi, G.; Arjun, M.; Yamuna, R. Synthesis, characterization and photoluminescence properties of tetra(aminophenyl) porphyrin covalently linked to multi-walled carbon nanotubes. *J. Chem. Sci.* **2017**, *129*, 699–706.

[15] Palacios-Pineda, L.; Perales-Martinez, I.; Lozano-Sanchez, L.; Martínez-Romero, O.; Puente-Córdova, J.; Segura-Cárdenas, E.; Elías-Zúñiga, A. Experimental investigation of the magnetorheological behavior of PDMS elastomer reinforced with iron micro/nanoparticles. *Polymers* **2017**, *9*, 696.

[16] Kumar, S.; Bayarkhuu, B.; Ahn, H.; Cho, H.; Byun, J. Photocatalytic H_2O_2 production in controlled oxidative environments using covalent triazine frameworks. *Nano Trends* **2023**, *4*, 100023.

[17] Chen, Z. K.; Shen, Z. L.; Zhang, X. Y.; Chen, L.; Hu, B. C.; Xu, G. Q.; Gao, C.; Xu, Q. H. Boosting photocatalytic H_2O_2 production by

fluorination of covalent organic frameworks via synergic charge transfer and phase regulation. *Appl. Catal. B: Environ. Energy* **2025**, *379*, 125731.

[18] Wang, Y.; Zhao, Y.; Liang, C.; Chen, Y.; Zhang, Q. Y.; Li, X. Y. Molecular-level modeling investigation of *n*-decane pyrolysis at high temperature. *J. Anal. Appl. Pyrolysis.* **2017**, *128*, 412–422.

[19] Wen, B. Y.; Sun, C. Z.; Bai, B. F.; Gatapova, E. Y.; Kabov, O. A. Ionic hydration-induced evolution of decane-water interfacial tension. *Phys. Chem. Chem. Phys.* **2017**, *19*, 14606–14614.

[20] Zhang, Y. N.; Pan, C. S.; Bian, G. M.; Xu, J.; Dong, Y. M.; Zhang, Y.; Lou, Y.; Liu, W. X.; Zhu, Y. F. H_2O_2 generation from O_2 and H_2O on a near-infrared absorbing porphyrin supramolecular photocatalyst. *Nat. Energy* **2023**, *8*, 361–371.

[21] Zhang, H.; Liu, M.; Zhang, X. Y.; Yuan, B.; Wu, P.; Liu, C. J.; Jiang, W. On-site H_2O_2 production with amphiphilic g-C_3N_4 as photocatalyst in a combined photocatalysis-extraction-separation process. *Chem. Eng. J.* **2022**, *438*, 135664.

[22] Das, P.; Roeser, J.; Thomas, A. Solar light driven H_2O_2 production and selective oxidations using a covalent organic framework photocatalyst prepared by a multicomponent reaction. *Angew. Chem., Int. Ed.* **2023**, *62*, e202304349.

[23] Galhenage, T. P.; Hoffman, D.; Silbert, S. D.; Stafslien, S. J.; Daniels, J.; Miljkovic, T.; Finlay, J. A.; Franco, S. C.; Clare, A. S.; Nedved, B. T. et al. Fouling-release performance of silicone oil-modified siloxane-polyurethane coatings. *ACS Appl. Mater. Interfaces.* **2016**, *8*, 29025–29036.

[24] Liu, J.; Qiu, W. T.; Dou, S.; Shang, H. J.; Zhang, Y. N.; Xu, J.; Zhang, J. W.; Lou, Y.; Zhang, Y.; Zhu, Y. F. et al. Quartz wool-supported porphyrin supramolecular photocatalysts for robust and scalable H_2O_2 generation. *EES Sol.* **2025**, *1*, 1115–1125.

[25] Yuan, Q.; Zhang, G. M.; Li, C. X.; Xu, S. W.; He, L. P. Effect of amino silicone oil-phosphorylation hybrid modification on the properties of microcellulose fibers. *Polymers* **2024**, *16*, 1123.

[26] Poursaberi, T.; Hassanisadi, M.; Torkestani, K.; Zare, M. Development of zirconium(IV)-metalloporphyrin grafted Fe_3O_4 nanoparticles for efficient fluoride removal. *Chem. Eng. J.* **2012**, *189–190*, 117–125.

[27] Chen, W. T.; Luo, Z. G.; Chen, H. L.; Kuang, H. M.; Liu, D. S. A novel porphyrin with a two-dimensional topology and highly thermal stability. *J. Chem. Res.* **2012**, *36*, 72–74.

[28] Piccirillo, G.; Moreira-Santos, M.; Válega, M.; Eusébio, M. E. S.; Silva, A. M. S.; Ribeiro, R.; Freitas, H.; Pereira, M. M.; Calvete, M. J. F. Supported metalloporphyrins as reusable catalysts for the degradation of antibiotics: Synthesis, characterization, activity and ecotoxicity studies. *Appl. Catal. B: Environ.* **2021**, *282*, 119556.

[29] Yang, B.; Niu, K. F.; Haag, F.; Cao, N.; Zhang, J. J.; Zhang, H. M.; Li, Q.; Allegretti, F.; Björk, J.; Barth, J. V. et al. Abiotic formation of an amide bond via surface-supported direct carboxyl-amine coupling. *Angew. Chem., Int. Ed.* **2022**, *61*, e202113590.

[30] Zhang, C. H.; Cao, M.; Jiang, S. J.; Huang, X. B.; Mai, K.; Yan, K. Quick analysis of composition of semi-aromatic copolyamide via ^{13}C NMR study. *Int. J. Polym. Anal. Charact.* **2019**, *24*, 40–53.

[31] Huang, Q.; Yu, J. G.; Cao, S. W.; Cui, C.; Cheng, B. Efficient photocatalytic reduction of CO_2 by amine-functionalized g-C_3N_4. *Appl. Surf. Sci.* **2015**, *358*, 350–355.

[32] Zhao, X. S.; You, Y. Y.; Huang, S. B.; Wu, Y. X.; Ma, Y. Y.; Zhang, G.; Zhang, Z. H. Z-scheme photocatalytic production of hydrogen peroxide over $Bi_4O_5Br_2$/g-C_3N_4 heterostructure under visible light. *Appl. Catal. B: Environ.* **2020**, *278*, 119251.

[33] Kanani-Jazi, M. H.; Akbari, S. Amino-dendritic and carboxyl functionalized halloysite nanotubes for highly efficient removal of cationic and anionic dyes: Kinetic, isotherm, and thermodynamic studies. *J. Environ. Chem. Eng.* **2021**, *9*, 105214.

[34] Chen, X. Y.; Wu, J. H.; Wang, X. Z.; Jia, R. R.; Li, L.; Wang, Y. X.; Cai, Y. X.; Chen, Z.; Jin, C. C.; Wang, X. Q. et al. Molecule self-assembly of hydrangea-shaped hollow O, Cl-codoped graphite-phase carbon nitride microspheres for efficient N-(1,3-dimethyl butyl)-N'-phenyl-p-phenylenediamine quinone photodegradation and bacteria disinfection. *J. Colloid Interface Sci.* **2025**, *683*, 1049–1056.

[35] Zhang, W. N.; Zhang, M. Y.; Wang, K.; Sun, R. X.; Zhao, S. L.; Zhang, Z. Q.; He, Y. P.; Yu, P. Geometry transformation of ionic surfactants and adsorption behavior on water/n-decane-interface: Calculation by molecular dynamics simulation and DFT study. *RSC Adv.* **2021**, *11*, 28286–28294.

[36] Zhang, X. C.; Cheng, S. L.; Chen, C.; Wen, X.; Miao, J.; Zhou, B. X.; Long, M. C.; Zhang, L. Z. Keto-anthraquinone covalent organic framework for H_2O_2 photosynthesis with oxygen and alkaline water. *Nat. Commun.* **2024**, *15*, 2649.

[37] Wang, S. D.; Xie, Z. P.; Zhu, D.; Fu, S.; Wu, Y. S.; Yu, H. L.; Lu, C. Y.; Zhou, P. K.; Bonn, M.; Wang, H. I. et al. Efficient photocatalytic production of hydrogen peroxide using dispersible and photoactive porous polymers. *Nat. Commun.* **2023**, *14*, 6891.

[38] Peng, H. P.; Yang, H. C.; Han, J. J.; Liu, X. Z.; Su, D.; Yang, T.; Liu, S. H.; Pao, C. W.; Hu, Z. W.; Zhang, Q. B. et al. Defective $ZnIn_2S_4$ nanosheets for visible-light and sacrificial-agent-free H_2O_2 photosynthesis via O_2/H_2O redox. *J. Am. Chem. Soc.* **2023**, *145*, 27757–27766.

[39] Xie, K. H.; Wang, G. B.; Huang, F.; Zhao, F.; Kan, J. L.; Chen, Z. Z.; Cai, L.; Han, S. L.; Geng, Y.; Dong, Y. B. Multicomponent one-pot construction of benzo[f]quinoline-linked covalent organic frameworks for H_2O_2 photosynthesis. *Nat. Commun.* **2025**, *16*, 3493.

[40] Liu, L. L.; Cui, C.; Chen, F.; Chen, J. J.; Yu, H. Q.; Xiong, Y. J. Recyclable quasi-homogeneous carbon nitride colloidal catalyst for sustainable photocatalytic H_2O_2 generation. *Angew. Chem., Int. Ed.* **2025**, *64*, e202508718.

[41] Gao, Z. X.; Liu, F. Y.; Chen, Z. W.; Song, Q.; Cullen, P. J.; Zhang, X. Y.; Zuo, Z. H.; Zhong, J.; Lu, X. Z.; Hu, Z. F. et al. Defect-modulated oxygen adsorption and Z-scheme charge transfer for highly selective H_2O_2 photosynthesis in pure water. *Nat. Commun.* **2025**, *16*, 8889.

[42] Ma, H. L.; Zhang, Y. P.; Wu, Y.; Gu, Q. F.; Li, Z. H.; Zhang. Q. C. Regulation of charge carrier transportation in D-π-A type covalent organic frameworks for promoting photocatalytic H_2O_2 production. *Chem. Sci.* **2025**, *16*, 16668–16677.

[43] Blatt, E.; Chatelier, R. C.; Sawyer, W. H. Effects of quenching mechanism and type of quencher association on Stern-Volmer plots in compartmentalized systems. *Biophys. J.* **1986**, *50*, 349–356.

[44] Vencel, T.; Donovalová, J.; Gáplovský, A.; Kimura, T.; Toma, Š. Oxygen exclusion from the organic solvents using ultrasound and comparison with other common techniques used in photochemical experiments. *Chem. Pap.* **2005**, *59*, 271–277.

[45] Zhang, J.; Xue, F.; Wang, Z. G. Insight into fluorine-nitrogen synergistic modification on covalent organic frameworks for efficient H_2O_2 synthesis by visible light catalysis. *Small* **2025**, *21*, e10448.

[46] Liu, Q.; Bi, H.; Zhao, R.; Yang, X. W.; Chen, F. Y.; Shen, Z. R. Fully exposed silver clusters enabling highly efficient photocatalytic H_2O_2 production in pure water. *Angew. Chem., Int. Ed.* **2025**, *137*, e202511687.

[47] Fang, L.; Xu, H.; Qiu, S. Y.; Ye, T.; Wang, T. Q.; Shang, J.; Gu, C.; Kitagawa, S.; Li, L. C. Autocatalytic interfacial synthesis of self-standing amide-linked covalent organic framework membranes. *Angew. Chem., Int. Ed.* **2025**, *64*, e202423220.

[48] Fang, L.; Qiu, S. Y.; Xu, H.; Ye, T.; Li, L. C. Encapsulation of single-atoms into covalent organic frameworks for highly efficient and persistent H_2O_2 photosynthesis via biphasic flow chemistry. *Adv. Funct. Mater.* **2025**, *35*, 2504676.